ADVANCED MATERIALS
www.advmat.de

20.64% Efficient and Stable Binary Organic Solar Cells via Thermodynamic-Engineered Interlayer Diffusion and Exciton Generation

Kangbo Sun, Yufei Wang, Guangye Zhang,* Chuanlin Gao, Xiwen Ling, Jianan Zheng, Jiaxu Che, Chen Xie, Zhibo Wang, Huawei Hu, Peng You, Peigang Han, Shunpu Li, and Yiwang Chen**

Despite thermodynamics playing a central role in active-layer optimization, unresolved temperature-dependent mechanisms hinder further efficiency improvements in organic solar cell. Herein, real-time thermal imaging is employed to unravel the temperature-controlled assembly dynamics during sequential processing (SqP) of active-layer films on a hot-substrate (HS). The HS process provides higher temperature and prolonged heating time for the active layer during SqP compared to the widely adopted hot-solution technique, enabling accelerated liquid-phase reorganization and nucleation in the bottom layer. The HS-induced interfacial energy difference promotes layer interpenetration and achieves suitable donor content in the bottom region of the active layer while boosting exciton generation. The highly crystalline fibrous structure improves hole mobility and suppresses non-radiative recombination (0.214 eV), yielding a high fill factor (81.00%) and open-circuit voltage (0.868 V). The 100 nm-thick D18 HS/eC9 device achieves an efficiency of 19.75% (vs 18.89% for the control) and retains 90% of its initial efficiency after 270 h under ≈1 sun illumination (vs 84% for the control). With 2PACZ as the hole transport layer, over 20% efficiency is demonstrated in three systems: 20.02% (D18/eC9-4F), 20.25 (D18/eC9), and 20.64% (D18/L8-BO, certified 20.10%). Notably, HS-processed 300 nm-thick binary devices achieve over 18.12% efficiency—among the highest reported.

1. Introduction

Organic solar cells (OSCs), capable of direct light-to-electricity conversion, have garnered significant research interest owing to their unique advantages, including lightweight, semi-transparency, flexibility, and robust mechanical stability.[1–6] Recent advances in non-fullerene acceptors, particularly those with strong nea-infrared absorption and high extinction coefficients, have propelled the power conversion efficiency (PCE) of OSCs beyond 21%.[7–11] State-of-the-art high-performance photovoltaic systems predominantly utilize wide-bandgap donor polymers PM6 and D18, both featuring a rigid planar benzodithiophene core, which facilitates efficient π–π stacking and high hole mobility.[12–20] The deeper highest occupied molecular orbital level of D18-based polymer donors versus PM6 enables higher open-circuit voltage (V_{OC}) values with Y-series non-fullerene small-molecule acceptors (NFSAs), thereby granting D18-based devices a PCE advantage over PM6-based systems under identical conditions.[21–25]

However, the ultra-high crystallization tendency of D18 that extended planar and rigid conjugated backbone also results in poor solubility and strong temperature-dependent aggregation behavior in most organic solvents.[26–28] Thus, hot solution spin-coating (e.g., ≈100 °C) has been widely adopted for disrupting the interchain π–π stacking to inhibit pre-aggregation in D18 solution, thereby improving film uniformity and enhancing workability.[29] In NFSAs system, dissolution at elevated temperatures followed by solution deposition conditions promotes excessive phase separation, leading to impaired exciton dissociation, intensified non-radiative recombination, and consequently, substantial V_{OC}

K. Sun, Y. Wang, G. Zhang, C. Gao, X. Ling, J. Zheng, J. Che, C. Xie, P. You, P. Han, S. Li
College of New Materials and New Energies
Shenzhen Technology University
Shenzhen 518118, China
E-mail: wangyufei@sztu.edu.cn; zhangguangye@sztu.edu.cn

The ORCID identification number(s) for the author(s) of this article can be found under https://doi.org/10.1002/adma.202509806

DOI: 10.1002/adma.202509806

Z. Wang, H. Hu
State Key Laboratory for Modification of Chemical Fibers and Polymer Materials
College of Materials Science and Engineering
Donghua University
Shanghai 201620, China

Y. Chen
College of Chemistry and Chemical Engineering/Institute of Polymers and Energy Chemistry
Nanchang University
Nanchang 330031, China
E-mail: ywchen@ncu.edu.cn

degradation.[30–33] Alternatively, the sequential deposition (SqP) is often employed for independently fabricating D18 donor layer (casted by hot solution) and Y-series NFSAs (prepared at room temperature) to enhance the whole device reproducibility.[16,34–38] When employing low-boiling-point chloroform (≈61.3 °C) as the processing solvent for active layer, the hot-solution method causes progressive concentration of the D18 precursor solution during successive spin-coating times, ultimately leading to substantial variations in thin-film thickness across different fabrication batches. Second, the interfacial thermodynamics between the substrate and hot D18 precursor solution remain poorly understood, particularly their potential influence on the surface property of casted D18 film. This interfacial incompatibility impedes the effective penetration of the upper acceptor layer into the underlying donor phase through critical swelling-induced diffusion,[35,39] resulting in a significant exciton loss. Consequently, additional post-treatment is typically required to heal these kinetically trapped defects and enhance overall film crystallinity, inevitably increasing manufacturing costs.

In this work, we reveal the thermal-regulation mechanisms governing SqP film active layers casted by hot substrate (HS) methodology. The HS method enables prolonged thermal driving force during the whole SqP film formation, effectively shortening the donor liquid-phase duration while accelerating D18 molecular nucleation, ultimately yielding robust bulk heterojunction film. Compared to pristine condition, the HS process substantially reduces the surface energy disparity between donor and acceptor films, leading to an easier penetration of upper acceptor molecules into the underlying polymeric donor matrix. As a result, HS-processed SqP films achieve optimized donor concentration profiles in the bottom region, dramatically improving exciton generation near the PEDOT:PSS interface and thereby enhancing photocurrent. Furthermore, the highly crystalline fibrous structure not only provides excellent hole mobility but also significantly suppresses non-radiative recombination losses within devices. The 100 nm-thick D18 HS/eC9-4F devices fabricated with conventional PEDOT:PSS hole transport layers exhibit outstanding photovoltaic performance: a V_{OC} of 0.868 V, short-circuit current density (J_{SC}) of 28.10 mA cm^{-2}, fill factor (FF) of 81.00%, and PCE of 19.75%. These devices also demonstrate exceptional photostability, maintaining 90% of their initial PCE after 270 h of continuous 1-sun illumination. When employing high-performance 2PACZ as the hole transport material, we obtained >20% PCE in 3 different material combinations: the champion devices based on D18/eC9, D18/eC9-4F and D18/L8-BO achieve record PCEs of 20.25%, 20.02%, and 20.64%, respectively (with the latter being certified at 20.10%). Notably, the HS process shows unique advantages in thick-film device fabrication, with 300 nm-thick binary devices reaching an unprecedented efficiency of 18.12%, representing one of the highest values reported to date in this field.

2. Results and Discussion

In this study, we constructed the photoactive layer using the D18 donor and non-fullerene acceptor eC9, with their molecular information and final device structure illustrated in **Figures 1a** and S1 (Supporting Information). Figure 1b schematically compares the conventional SqP method with our HS approach, where HS was exclusively applied to the bottom D18 film deposition unless otherwise noted. To characterize the thermal dynamics, we employed high-resolution thermal imaging to monitor surface temperature evolution during film fabrication. To characterize the temperature change, we employed high-resolution thermal imaging to monitor the surface temperature evolution during film fabrication. Herein, thermal imaging characterization was performed using a mobile thermal imager (FLUKE, TC01A) with a resolution of 256 × 192 pixels. Thermal imaging recording was initiated immediately after placing the sample on the spin coater's vacuum chuck. For the hot-substrate method, substrates were first heated on a hot plate at 70 °C for ≈5 min and then promptly transferred to the spin-coater's vacuum chuck. All measurements were performed on silicon wafers to eliminate temperature artifacts from ITO glass heterogeneity. The representative thermal images at key spin-coating intervals during HS-casted SqP process are presented in Figure 1c, the conventional fabrication process is monitored in Figure S2 (Supporting Information). The recorded detailed temperature change during SqP process can be seen in the Movie Files 1–3. Later, we extracted complete temperature-time profiles, as shown in Figure 1d. It can be seen that all SqP samples exhibited three distinct thermal regimes: substrate pre-rotation stage (blue region), D18 deposition process (yellow region) and upper eC9 spin-coating process. In conventional preparation processes, the D18/eC9 film surface maintained exceptional thermal stability, with temperature variations consistently constrained within a 3 °C range throughout the entire fabrication procedure. During the pre-spin coating stage (1–12s), frictional heating due to high-speed rotation between the substrate and the surrounding air leads to a marginal temperature rise, increasing the surface temperature from 29.7 °C to 30.6 °C. The deposition process of D18 and eC9 solutions leads to surface temperature reduction, occasionally causing the temperature to dip below the ambient level. This transient cooling effect lowered ambient temperature is attributed to the endothermic evaporation of the D18 or eC9 solvent, which extracts thermal energy from the film surface during the deposition process.

In contrast, the HS process exhibited significantly greater temperature variation range (31 °C – 59.1 °C). During bare substrate spinning, the temperature showed a rapid drop from 59.1 to 54.9 °C within the first 3 s (cooling rate: ≈1.33 °C s^{-1}), transitioning to a stable linear decay phase (1.00 °C s^{-1}) between 4 and 8 s. For the second stage, introduction of room-temperature D18 solution caused an immediate temperature plunge to 42.4 °C, resulting from both ambient cooling and solution-substrate thermal equilibration. Subsequently, the cooling rate progressively decreased from 0.5 to 0.2 °C s^{-1} as spin-coating continued (12–29 s). In the last stage, spin-coating of the eC9 solution triggered a characteristic temperature drop from 36.4 to 31 °C, followed by stabilization at ambient temperature (32.8 °C). Indeed, for the HS method, the critical parameter requiring precise control is the substrate temperature at the moment of D18 solution contact, rather than the initial substrate temperature when placed on the spin-coater chuck (previously measured at 59.1 °C). Theoretically, the initial substrate temperature can be adjusted freely, as long as the optimal contact temperature (≈50 °C) for the D18 solution is achieved. This optimum temperature was identified through systematic device performance optimization, as detailed

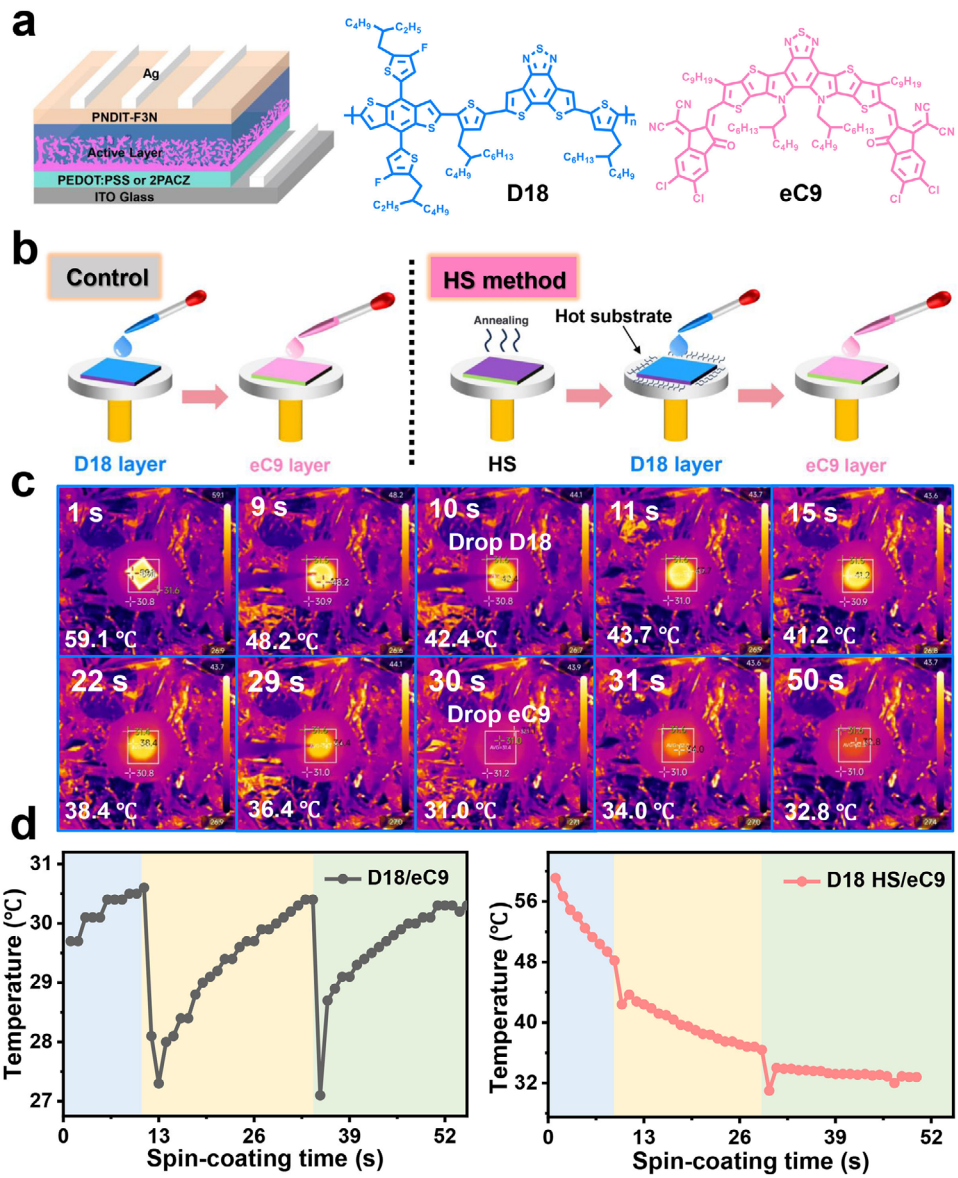

Figure 1. a) Device schematic and chemical structures of the active layer materials employed in this study. b) Schematic illustration of the conventional (control) and HS methods for preparing SqP D18/eC9 film. c) Temperature evolution images of the SqP film surface during the HS process with spin-coating time. d) Time-dependent surface temperature profile of the substrate during the whole SqP film fabrication process.

in later sections. Herein, we conducted further comparative measurements on conventional hot D18 solution (80 °C) fabricated SqP films, and the subsequent processing steps for the eC9 solution remained unchanged (Figures S3 and S4, Supporting Information). However, the instrument's thermal imaging rate (>1 s/frame) precluded detection of measurable temperature variations during the entire hot D18 solution casted SqP film process. This observation indicates that the thermal variation period during hot-solution processed D18/eC9 film formation under high-speed spinning conditions may shorter than 1 s. Comparative studies with hot-solution processed D18/eC9 films revealed that the HS method extends thermal modulation timescales (>30 s vs <1 s for conventional processing) at equivalent temperatures. This prolonged thermal control likely suppresses premature D18 aggregation more effectively during film formation.[29] For actual devices fabricated on ITO substrates, we also evaluated SqP films prepared using the three methods including ambient-temperature fabrication (D18/eC9), HS method (D18 HS/eC9), and hot-solution technique (D18 hot-solution/eC9), as shown in Figure S5 (Supporting Information). Although the differences in thermal conductivity and heat capacity between silicon and ITO glass led to a temperature discrepancy (≈9 °C higher for ITO) between the two substrates under ambient conditions, the overall temperature fluctuations during the preparation of SqP films—whether by ambient or hot-solution processing—remained minimal (within 4 °C). Notably, for the HS process, the initial surface temperatures and their subsequent evolution exhibited nearly identical trends on both ITO and silicon substrates. This

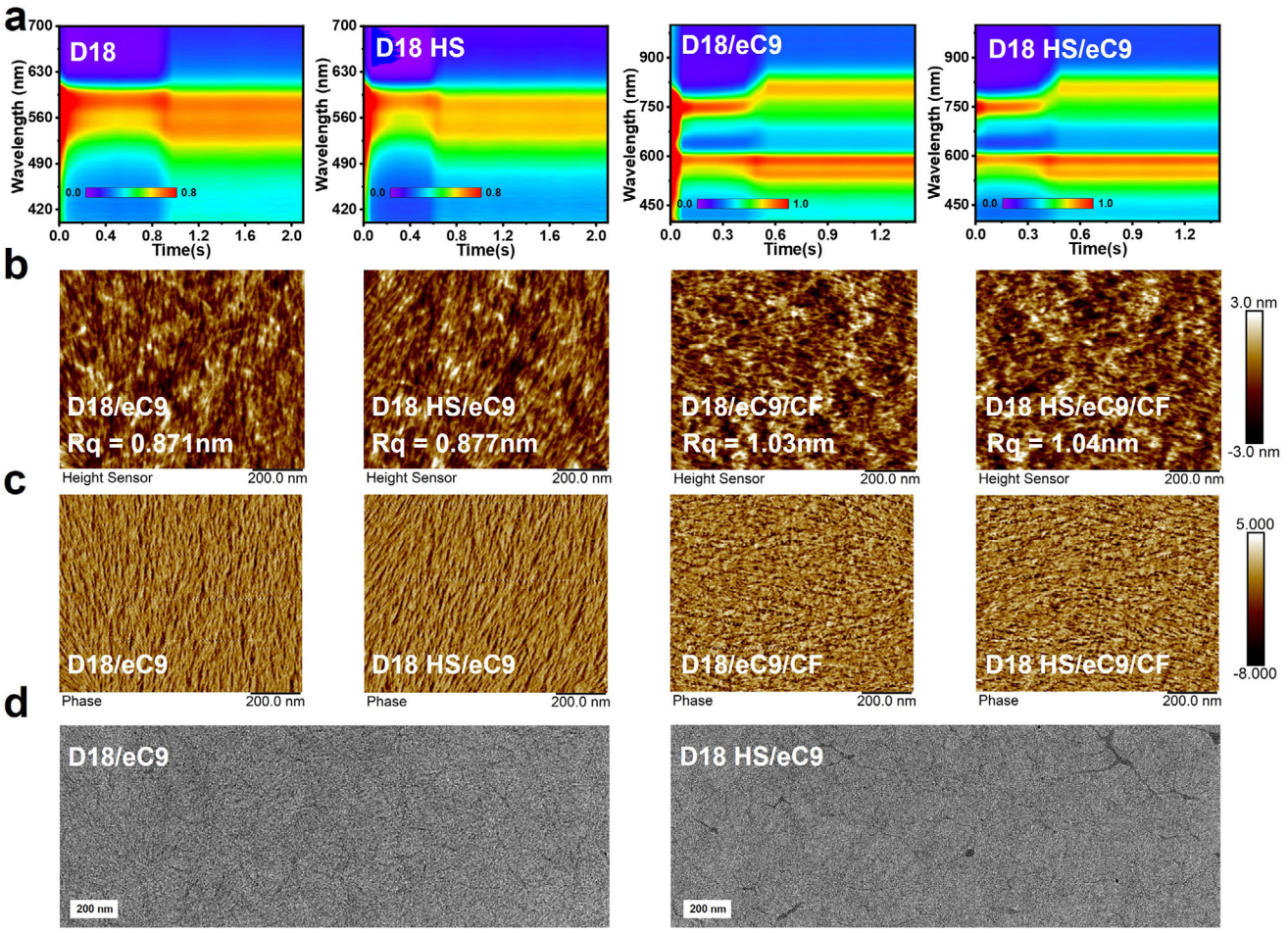

Figure 2. a) In situ 2D absorption spectroscopy monitoring the formation of D18 and D18/eC9 films during spin-coating. The horizontal scale bar denotes absorption intensity. b) AFM height images and c) the corresponding phase images of the D18/eC9 films processed without and with the HS method. d) TEM micrographs of D18/eC9 films before and after HS pre-treatment.

remarkable consistency strongly validates the reliability of our conclusions.

Using the two-liquid method and Owen's equation,[40] we evaluated the surface energy (γ) of D18/eC9 films fabricated via the conventional SqP method and the HS approach (Figure S6 and Table S1, Supporting Information). The total γ of the solid films comprises polar and dispersion components. For films prepared by the conventional technology, the γ values of D18 and eC9 were 25.12 and 29.97 mN m^{-1}, respectively. This significant surface energy difference between the donor (D18) and acceptor (eC9) layers in the SqP process likely hinders effective interlayer penetration during swelling process.[41] In contrast, the HS-treated D18 film exhibited a γ of 26.55 mN m^{-1}, closer to that of eC9 (29.97 mN m^{-1}). Moreover, the final D18 HS/eC9 SqP film showed a reduced γ of 27.16 mN m^{-1} compared to the pristine D18/eC9 film (28.47 mN m^{-1}), approaching the value of the underlying D18 HS layer. This shift suggests a higher D18 content on the film surface, consistent with enhanced interlayer mixing. These results demonstrate that the HS process reduces the interfacial energy mismatch between layers, promoting more thorough swelling of the upper acceptor (eC9) into the underlying donor (D18) film.

In situ absorption spectroscopy was utilized to investigate the dynamic evolution of optical properties during the spin-coating process of D18/eC9 films, with particular emphasis on comparing the two processing methods for the bottom D18 layer fabrication. Time-resolved 2D absorption spectra and selected characteristic absorption profiles are displayed in **Figures** 2a and S7a,b (Supporting Information), respectively. Herein, the film formation process of D18 hot-solution spin coating on room temperature ITO substrate was also tested as a comparison (Figure S7c,d, Supporting Information). Quantitative analysis of the film formation kinetics, including liquid-phase duration and nucleation time, is presented in Figure S8 (Supporting Information).[42,43] The HS method casted D18 film obtained a smallest liquid-phase duration of 490 ms, which is remarkably lowered than pristine method (700 ms) and hot-solution technology (700 ms). The result indicated that the HS process can inhibit D18 pre-aggregation in the solution state, which is consistent with the observed the slightly blue-shift absorption edge in final D18 film (Figure S9, Supporting Information). Compared with conventional method, HS and hot solution technique accelerated nucleation kinetics of D18 molecule, decreasing the crystallization

onset time by 40% (210 ms vs 350 ms). During the critical swelling stage (measured as shown in Figure 2a; Figures S10 and S11, Supporting Information), where eC9 solution was spin-coated onto bottom D18 films, both processing methods exhibited consistent secondary donor nucleation (140 ms) and acceptor nucleation (280 ms) timescale independent of the underlying donor film.[44] The HS-treated or hot solution fabricated SqP films demonstrated a shortened D18 secondary liquid—phase duration (350 ms) and reduced acceptor liquid-phase time (210 ms), which represents a fast swelling process between upper eC9 and bottom D18 layer.

To elucidate the structure-property relationships, we systematically investigated the surface and bulk morphologies of both conventional and HS-processed D18 or SqP films using atomic force microscopy (AFM) and transmission electron microscopy (TEM) (Figure 2b–d). Figure 2b,c displays representative AFM height images of the SqP film surfaces and corresponding phase images. Following HS treatment, the D18 films demonstrated a measurable increase in root-mean-square roughness (Rq) from 1.07 to 1.17 nm, accompanied by the development of uniformly distributed and coarser fibrous structures (Figure S12, Supporting Information). While HS-treated D18 films displayed increased surface roughness, subsequent eC9 deposition yielded final SqP films with comparable Rq values to conventional D18/eC9 films (0.877 nm vs 0.871 nm), with both maintaining optimal interfacial contact with the electron transport layer. TEM analysis confirmed the presence of these characteristic coarse fibers in HS-treated D18 films (Figure S13, Supporting Information), which remained structurally intact in the corresponding D18 HS/eC9 SqP films. These observations indicate that eC9 molecules likely infiltrate the underlying donor phase by navigating around the coarse D18 fiber structures. Following chloroform (CF) rinsing, AFM results revealed comparable surface roughness values of 1.15 and 1.13 nm for pristine and HS-treated D18 films (Figure S14, Supporting Information), respectively, while D18/eC9 and HS-treated D18/eC9 blend films exhibited slightly reduced Rq values of 1.03 and 1.04 nm (Figure 2b,c). Moreover, the fibrous morphology was almost completely eliminated in the these SqP films after CF treatment, whereas distinct fibrous features persisted in the CF-washed D18 control film. To gain further insight into these morphological changes, we conducted UV–vis absorption spectroscopy to analyze the films before and after CF treatment (Figure S15, Supporting Information). Both pristine D18 and HS-treated D18 films showed minimal spectral changes, with only slight intensity reductions while maintaining their original spectral profiles. Among them, the absorption spectral intensity of the HS-treated D18 film after CF washing decreases more significantly, suggesting that the subsequently deposited upper eC9 acceptor would achieve more thorough intermixing with the underlying D18 layer. In striking contrast, SqP films demonstrated dramatic spectral alterations using CF treatment, including: 1) substantial intensity reduction across all wavelengths, and 2) near-complete elimination of eC9's characteristic absorption features (670–900 nm), confirming the fact of acceptor composition disappearance. Interestingly, HS-processed films exhibited enhanced bulk heterojunction morphological stability against solvent washing, as evidenced by comparatively smaller absorption losses in D18/eC9 systems—a phenomenon we attribute to their coarser fibrous network providing strong support for the entire stable film skeleton.

To investigate the crystalline properties of the films, we conducted grazing-incidence wide-angle X-ray scattering (GIWAXS) measurements. The two-dimensional (2D) scattering patterns (**Figure 3a**) and corresponding out-of-plane (OOP) and in-plane (IP) line profiles (Figure S16, Supporting Information) provide comprehensive structural information. Quantitative analysis of key crystallographic parameters was performed, including crystal coherence length ($CCL = 2\pi$K/FWHM) and π–π stacking distance ($d_{\pi-\pi} = 2\pi/q$). These parameters were systematically compared across different processing conditions and summarized in Figure 3b,c and Table S2 (Supporting Information). For SqP films, the HS process led to reduced $d_{\pi-\pi}$ distances in both the IP (20.2 Å) and OOP (3.66 Å) directions, as compared to the control samples (20.4 and 3.69 Å, respectively).[12] Simultaneously, HS-treated D18/eC9 films exhibited increased *CCL* along both the Q_{xy} (106.7 Å) and Q_z (36.96 Å) directions,[45,46] which aligns with the "coarse fibrous" morphology revealed by AFM characterization. The D18 HS/eC9 system demonstrated slightly tighter π–π stacking and long *CCL* values, confirming enhanced molecular ordering that favors higher charge carrier mobility.[47,48]

Film-depth-dependent light absorption spectroscopy was employed to analyze vertical phase separation in SqP films through soft plasma etching of electrode-free samples (Figure S17, Supporting Information). By deconvoluting the absorption spectra with reference to pristine D18 and eC9 films (Figures S15 and S18, Supporting Information), we quantitatively reconstructed the donor/acceptor distribution ratio along the film depth (Figure 3d).[49,50] In the 0–60 nm region, D18 HS/eC9 films exhibited a high donor content compared to conventional films, attributable to enhanced acceptor penetration facilitated by the optimized surface energy matching ($\Delta\gamma = 3.42$ mN m^{-1}) between HS-treated D18 and eC9. While conventional SqP processing led to excessive D18 accumulation (79.46%) close to the PEDOT:PSS interface that primarily benefited hole transport at the expense of exciton generation, the HS-processed films achieved a suitable donor ratio (64.23%) that balanced both exciton generation and charge collection efficiency approaching PEDOT:PSS interface. Optical transfer matrix simulations confirmed the enhancement in exciton generation rates within the 60–100 nm region for HS-processed SqP films, thereby contributing to higher photocurrent generation (Figure 3e; Figure S19, Supporting Information).[50,51] These findings demonstrate that precisely controlled donor–acceptor interpenetration, achieved through surface energy optimization and moderate donor content reduction (near PEDOT:PSS), can simultaneously enhance exciton generation and charge collection efficiency.

To systematically evaluate the impact of HS method on the SqP OSCs, we fabricated photovoltaic devices (ITO/PEDOT:PSS/D18/eC9/PNDIT-F3N/Ag) and observed significant performance enhancements. Current density–voltage (*J*–*V*) measurements (**Figure 4a** and **Table 1**) revealed that HS-treated D18/eC9 devices achieved superior performance metrics compared to controls: V_{OC} improved from 0.857 to 0.868 V, J_{SC} increased from 27.75 to 28.10 mA cm^{-2}, and FF enhanced from 79.37% to 81.00%, collectively boosting the PCE from 18.89% to 19.75%. The detailed optimal process can be found in Figures S20 and S21 and Table S3 (Supporting

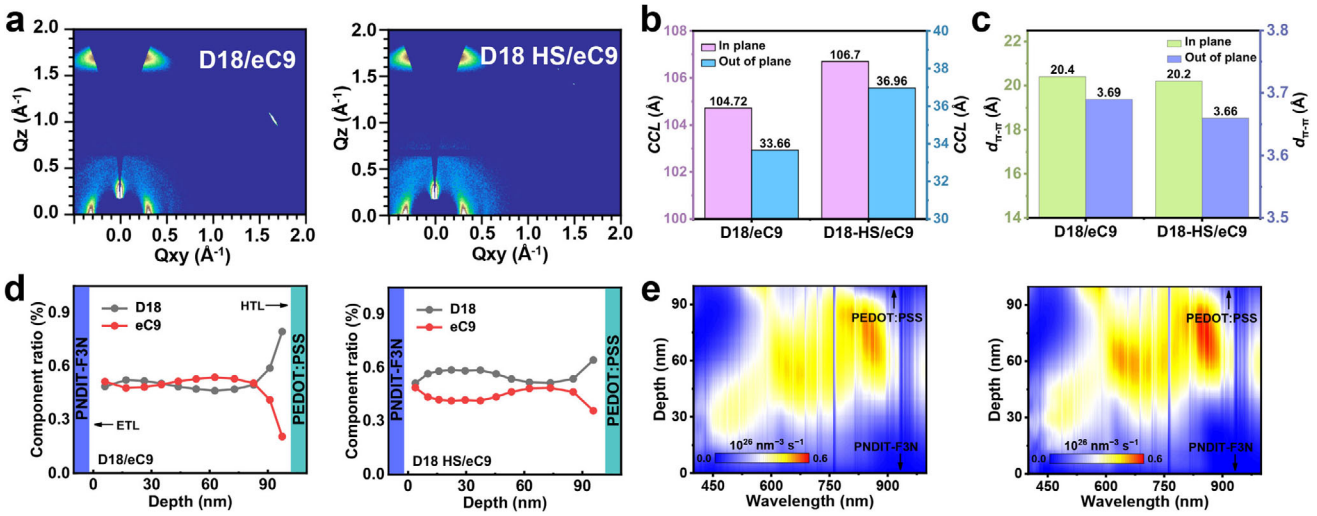

Figure 3. a) 2D GIWAXS patterns of pristine D18 and D18/eC9 blend films. b) *CCL* derived from 2D GIWAXS line-cut profiles. c) Comparative analysis of $d_{\pi-\pi}$ for D18 and SqP films in both IP and OOP orientations. d) Depth-dependent composition profiles across the vertical direction in active layer. e) Simulated exciton density distributions visualized through optical transfer matrix modeling, with scale bars indicating the maximum exciton generation rate.

Information). The <4% discrepancy between J_{SC} values from *J–V* and external quantum efficiency (EQE) measurements (Figure 4b) validated data reliability. For comparison, SqP devices fabricated via the hot-solution process alone demonstrated only a moderate PCE of 19.14% (Figure S22 and Table S4, Supporting Information). When combining the hot-solution with the HS method, the resulting devices exhibited further reduced performance, with a PCE of merely 18.36%, which was significantly lower than that of the control device (18.89%). To probe the charge recombination dynamics, we analyzed the light intensity (I_{light}) dependence of J_{SC} and V_{OC} (Figure 4c; Figure S23, Supporting Information). The relationships follow $J_{SC} \propto I_{light}^{\alpha}$ and $Voc \propto \frac{nkT}{q}\ln(I_{light})$, where α approaching 1 indicates suppressed bimolecular recombination, and n closes 1 suggests minimal trap-assisted recombination.[52] Recombination analysis through light intensity dependence yielded near-ideal parameters for HS-casted SqP devices (α = 1.047, n = 0.990) versus controls (α = 0.986, n = 1.118), indicating suppressed bimolecular and trap-assisted recombination.[53,54] Additionally, the influence of the HS technique on charge carrier dynamics was evaluated by performing transient photocurrent (TPC) and transient photovoltage (TPV) measurements on the operational OSC devices (Figure 4d,e). The results showed HS-treated OSCs exhibited 31.6% faster charge extraction (0.143 µs vs 0.209 µs) and 23.6% longer carrier lifetimes (2.968 µs vs 2.415 µs), confirming reduced bulk recombination. Dark current analysis (Figure S24, Supporting Information) demonstrated HS technique increased turn-on voltage (0.76 V vs 0.71 V) and reduced leakage current at reverse and forward biases, evidencing enhanced film quality.

To explore the charge transport dynamics in SqP OSCs, the impedance spectroscopy (IS) measurements are performed under open-circuit conditions, scanning frequencies from 100 Hz to 1 MHz (Figure 4f). Equivalent circuit fitting yielded key electrical parameters (Figure S25 and Table S5, Supporting Information). The fitted data revealed that HS-treated devices exhibited significantly reduced resistances, with active medium resistance (R_1) decreasing to 17.34 Ω and interface resistance (R_2) to 1694 Ω. This three-fold reduction in both bulk and interfacial resistances suggests substantial improvements in charge transport through the active layer and across electrode interfaces. Further insight into charge dynamics was obtained through photo-induced charge extraction by linearly increasing voltage (Photo-CELIV) and current-based deep-level transient spectroscopy (DLTS) measurements (Figure 4g; Figure S26, Supporting Information). The control devices showed ordinary carrier mobility (μ_{avg} = 7.30 × 10^{-5} cm^2 V^{-1} s^{-1}) and high trap density (N_t = 2.30 × 10^{15} cm^{-3}), while HS treatment enhanced μ_{avg} by 38% to 1.01 × 10^{-4} cm^2 V^{-1} s^{-1} and reduced N_t by 54% to 1.05 × 10^{15} cm^{-3}.[55,56] These improvements are advantageous for achieving a high FF and minimizing energy loss.[57] Space-charge-limited-current measurements of hole-only and electron-only devices provided additional transport characterization through Mott-Gurney analysis ($J = \frac{9\varepsilon_0\varepsilon_r\mu V^2}{8d^3}$) (Figure S27, Supporting Information; Figure 4h). The HS-induced fibrous morphology increased hole mobility in pristine D18 films from 6.69 × 10^{-4} to 8.79 × 10^{-4} cm^2 V^{-1} s^{-1}. More importantly, in complete SqP devices, HS processing indeed enhanced hole mobility from 3.89 × 10^{-4} to 5.28 × 10^{-4} cm^2 V^{-1} s^{-1}, achieving better charge balance with electron mobility (5.6 × 10^{-4} cm^2 V^{-1} s^{-1}). This optimized charge transport directly correlates with the improved J_{SC} (from 27.75 to 28.10 mA cm^{-2}) and FF (from 79.37% to 81.00%) in HS-processed D18/eC9 SqP devices. To illustrate the origin of the V_{OC} enhancement, we performed comprehensive analyses using electroluminescence external quantum efficiency (EL-EQE) and Fourier-transform photocurrent spectroscopy external quantum efficiency (FTPS-EQE) measurements (Figure S28 and Table S6, Supporting Information; Figure 4i). The total voltage loss (ΔE_{total}) was commonly decomposed into three components: (i

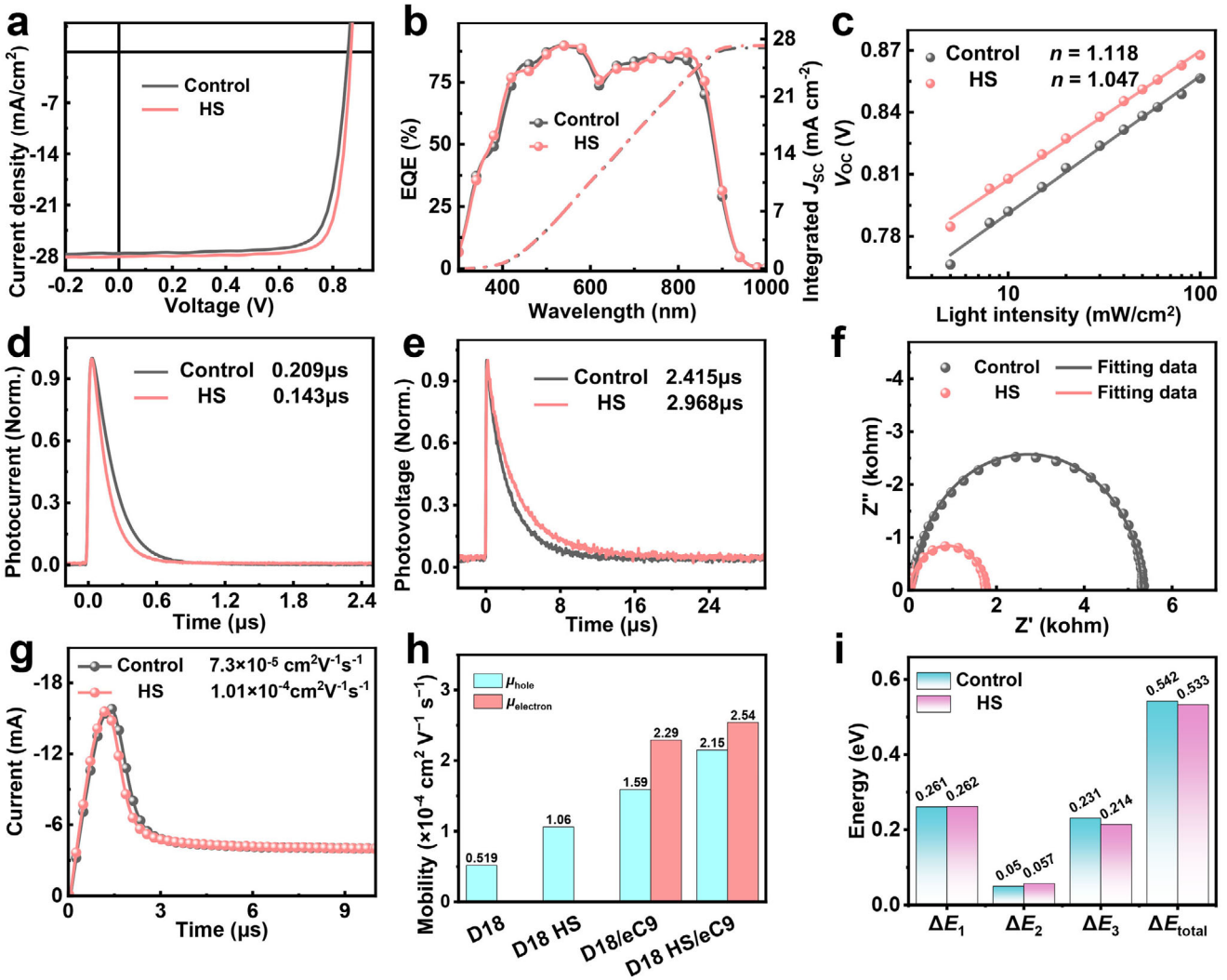

Figure 4. a) *J–V* characteristics under AM 1.5G illumination. b) EQE spectra with integrated current density values. c) V_{OC} as a function of I_{light}. d) TPC decay profile. e) TPV relaxation dynamics. f) Nyquist plots from impedance spectroscopy measurements. g) Photo-CELIV results. h) Comparison of mobility in D18 and D18/eC9 films processed with and without the HS method. i) E_{loss} analysis for pristine SqP devices and HS-treated D18/eC9 OSCs.

and ii) above-bandgap radiative losses of ΔE_1 (≈0.262 eV) and ΔE_2 (≈0.05 eV) that showed minimal variation among devices, and (iii) below-bandgap non-radiative losses (ΔE_3). Remarkably, the HS-treated devices demonstrated a significant reduction in ΔE_3 (0.214 eV) compared to control devices (0.231 eV), which directly contributed to their lower overall voltage loss and consequently higher V_{OC}.

Subsequently, the fabricated device operational stability was assessed by maximum power point tracking (MPPT) means under continuous 1-sun equivalent LED illumination (270 h). Control devices retained 85.76% of initial PCE, while substrate-preheated devices exhibited exceptional photostability with only ≈10% PCE degradation (**Figure 5a**). This enhanced stability originates from robust morphological frame in HS-processed SqP films, as verified by AFM and TEM analysis. Moreover, we demonstrate the broad universality of HS method, we tested other two high-performance systems and previous D18/eC9 device employing 2PACz as the hole transport layer alternative to conventional

Table 1. Photovoltaic parameters for the control or HS-casted D18/eC9 devices using PEDOT:PSS.

Condition	V_{OC}[V]	J_{SC} [mA cm^{-2}]	FF [%]	PCE [%]
Control[a)]	0.857	27.75 (26.94)[b)]	79.37	18.89[c)] (18.72[d)] ± 0.13)
HS method[a)]	0.868	28.10 (27.20)[b)]	81.00	19.75[c)] (19.63[d)] ± 0.10)

[a)] These SqP devices are fabricated based on PEDOT:PSS; [b)] Extracted Integrated current densities from EQE spectra; [c)] The highest PCE; [d)] The average PCE based on at least 5 independent devices.

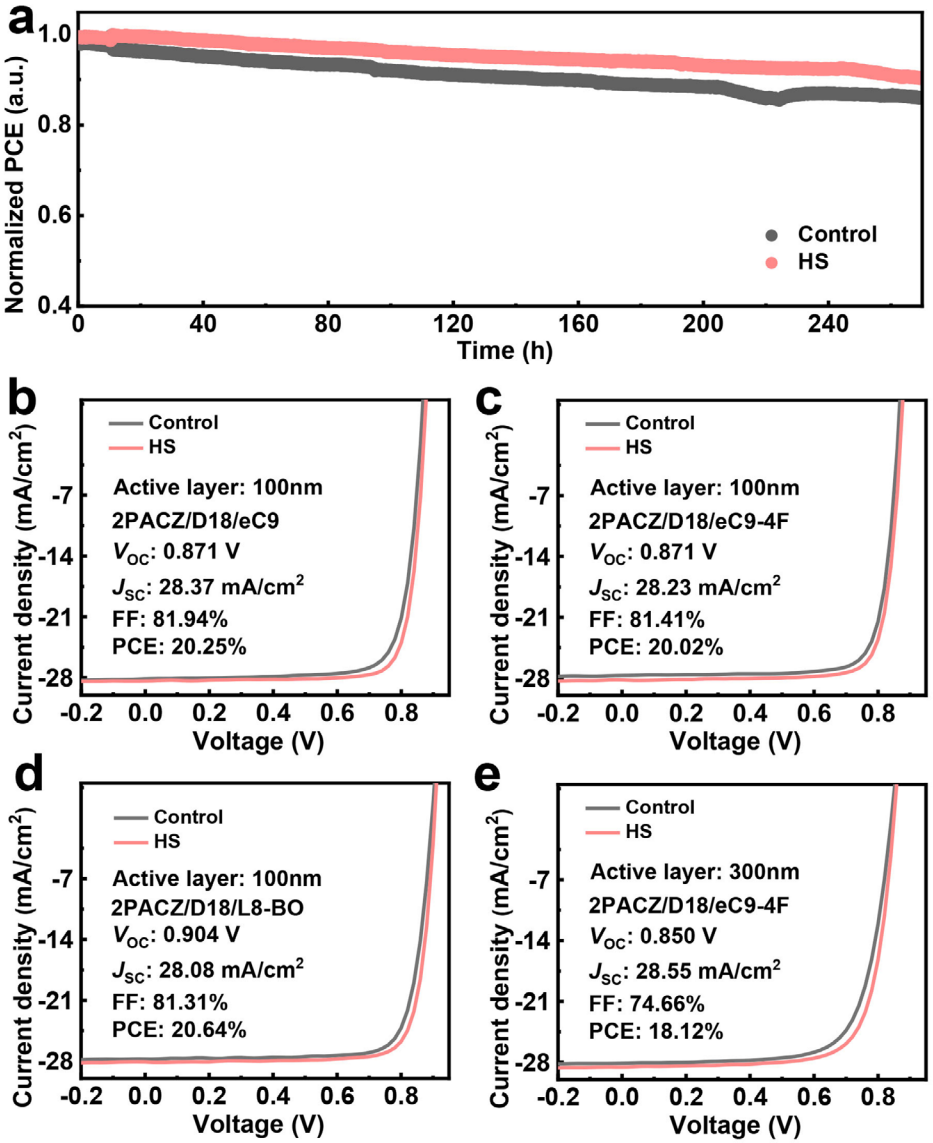

Figure 5. a) Photostability evaluation of D18/eC9 and D18 HS/eC9 devices under continuous MPPT over 270 h (LED illumination intensity: 100 mW cm^{-2}. b–e) *J–V* characteristics of four OSCs systems fabricated through the synergistic combination of 2PACz HTL and HS methodology.

PEDOT:PSS (Figure 5b–e; Figures S29–S33, Supporting Information; **Table 2**). The HS-processed D18/eC9 devices based on 2PACZ exhibited outstanding performance, achieving a champion PCE of 20.25% coupled with a remarkable FF of 81.94% compared with control device (PCE: 19.21%; FF: 79.2%). Furthermore, when applied to the D18/L8-BO system, our HS approach enabled SqP devices to attain an impressive PCE of 20.64% (Figure 5d; Figure S32, Supporting Information), which was independently certified at 20.10% by the South China National Metrology Center (Figure S34, Supporting Information), confirming the reliability and reproducibility of our methodology. Finally, we further explored the HS method's applicability to thick-film devices using the D18/eC9-4F system. For 100-nm active layers, HS-processed devices achieved a PCE of 20.02% (vs 19.30% for controls). When the thickness was increased to 300 nm, conventional SqP device yielded a poor PCE of 17.12% due to inferior FF (72.36%) and low J_{SC} (28.14 mA cm^{-2}). Remarkably, HS-processed devices maintained a high PCE of 18.12% at this thickness through simultaneous improvements in both FF (74.66%) and J_{SC} (28.55 mA cm^{-2}), representing one of the highest reported efficiencies for binary thick-film (≥300 nm) OSCs to date.

The enhanced photovoltaic performance in 2PACZ-based devices primarily originates from its deeper work function and the formation of longer crystalline coherence lengths in the active layer film induced by it.[58,59] These factors collectively improve charge transport while suppressing recombination, thereby achieving higher J_{SC} and FF values. Furthermore, we conducted systematic AFM measurements of the D18/eC9 films prepared on both PEDOT:PSS and 2PACZ-based substrates (Figure S35, Supporting Information). The active layer prepared on top of 2PACZ exhibited significantly higher RMS roughness compared to its PEDOT:PSS counterpart. This roughness difference

Table 2. Photovoltaic parameters of pristine and HS-treated SqP OSCs based on 2PACZ hole transport layer.

Active layer	Condition	V_{OC} [V]	J_{SC} [mA cm^{-2}]	FF [%]	PCE [%]
D18/eC9	Control[a)]	0.862	28.14 (27.00)[d)]	79.20	19.21[e)] (18.94[f)] ± 0.15)
	HS method[a)]	0.871	28.37 (27.21)[d)]	81.94	20.25[e)] (20.02[f)] ± 0.26)
D18/L8-BO	Control[a)]	0.897	27.78 (26.32)[d)]	79.77	19.88[e)] (19.57[f)] ± 0.21)
	HS method[a)]	0.904	28.08 (26.60)[d)]	81.31	20.64[e)] (20.33[f)] ± 0.31)
	HS method[a,b)]	0.887	28.08	80.67	20.10[e)]
D18/eC9-4F	Control[a)]	0.862	27.71 (26.70)[d)]	80.37	19.20[e)] (18.90[f)] ± 0.32)
	HS method[a)]	0.871	28.23 (27.01)[d)]	81.41	20.02[e)] (19.88[f)] ± 0.11)
	Control[c)]	0.841	28.14 (27.36)[d)]	72.36	17.12[e)] (16.91[f)] ± 0.24)
	HS method[c)]	0.850	28.55 (27.61)[d)]	74.66	18.12[e)] (18.00[f)] ± 0.19)

[a)] The thickness of active layer is 100 nm; [b)] Certified by the South China National Center of Metrology, China; [c)] The thickness of active layer is 300 nm; [d)] Integrated J_{SC} values from EQE spectra; [e)] The highest value of PCE; [f)] The average values of PCE are based on at least five independent devices.

persisted throughout sequential deposition of D18 and eC9. The enhanced surface roughness of 2PACZ/D18 films facilitates better penetration of the eC9 acceptor into the underlying layer, consequently improving exciton dissociation. Additionally, the higher roughness of 2PACZ/D18/eC9 films provides greater interfacial contact area, which may accelerate charge collection at the cathode.

3. Conclusion

In this work, we elucidate the fundamental thermal-regulation mechanisms governing the formation of high-performance SqP films via the HS methodology. Through precise thermal management, the HS process provides sustained thermal driving forces throughout film deposition, which simultaneously i) reduces the liquid-phase duration of D18 donors, ii) accelerates molecular nucleation kinetics, and iii) minimizes interfacial energy disparities between donor/acceptor components. These synergistic effects enable a more robust SqP film and achieve more sufficient interlayer permeation, which significantly enhances the generation of excitons at the bottom of the active layer. Meanwhile, the HS-induced coarser D18 fibrous structure provide tighter π–π stacking and long *CCL* values, significantly enhancing the mobility and suppressing non-radiative recombination. The HS method universally enables >20% PCE across all three D18-based systems, achieving a champion efficiency of 20.64% (certified 20.10%) in the D18/L8-BO systems. Notably, the HS methodology exhibits unprecedented thickness insensitivity, with 300-nm-thick binary devices attaining 18.12% efficiency, outperforming conventional processed devices (17.12%). The above performance ranks among the top reported values for 100 nm-film and thick-film (>250 nm) binary OSCs to date. This work highlights the pivotal role of thermodynamic control in active-layer optimization, where mechanistic understanding of thermal regulation provides a critical pathway for advancing OSCs performance beyond current limitation.

Supporting Information

Supporting Information is available from the Wiley Online Library or from the author.

Acknowledgements

The work was supported by the Guangdong Basic and Applied Basic Research Foundation (2025A1515012147), the National Natural Science Foundation of China (12404480), and the Shenzhen Science and Technology Program (JCYJ20240813113238050, JCYJ20240813113306008). S.P.L. would like to thank the Education Department of Guangdong Province (2021KCXTD045), the National Natural Science Foundation of China (12274303), the Shenzhen Key Laboratory of Applied Technologies of Super-Diamond and Functional Crystals (ZDSYS20230626091303007). The author also thanks the support from the National Natural Science Foundation of China (52103202), and beamline BL16B1 at Shanghai Synchrotron Radiation Facility (SSRF) for the GIWXS experiment.

Conflict of Interest

The authors declare no conflict of interest.

Author Contributions

K.B.S. and Y.F.W., and Y.G.Z. contributed equally to this work. K.B.S. and Y.F.W. designed the experiment and wrote the original manuscript. C.L.G. and X.W.L. carried out the in situ absorption and mobility measurements. J.N.Z. and J.X.C. provided the high-resolution thermal imaging measurement. C.X. and P.Y. contributed the device fabrication support and edited the original manuscript. Z.B.W. and H.W.H. provided GIWAXS measurement. Y.F.W. and G.Y.Z. provided original idea. Y.W.C. provided thermal dynamics analysis and edited the final manuscript. Y.F.W., P.G.Y.H., S.P.L., and G.Y.Z. revised the final manuscript and provided funding support.

Data Availability Statement

The data that support the findings of this study are available from the corresponding author upon reasonable request.

Keywords

device engineering, interlayer diffusion, non-radiative recombination, organic solar cells, sequential processing

Received: May 24, 2025
Revised: August 18, 2025
Published online:

[1] W. Kong, J. Wang, Y. Hu, N. Cui, C. Yan, X. Cai, P. Cheng, *Angew. Chem., Int. Ed.* **2023**, *62*, 202307622.
[2] R. Ma, B. Zou, Y. Hai, Y. Luo, Z. Luo, J. Wu, H. Yan, G. Li, *Adv. Mater.* **2025**, *37*, 2500861.
[3] B. Liu, W. Xu, R. Ma, J.-W. Lee, T. A. Dela Peña, W. Yang, B. Li, M. Li, J. Wu, Y. Wang, C. Zhang, J. Yang, J. Wang, S. Ning, Z. Wang, J. Li, H. Wang, G. Li, B. J. Kim, L. Niu, X. Guo, H. Sun, *Adv. Mater.* **2023**, *35*, 2308334.
[4] W. Gao, M. Jiang, Z. Wu, B. Fan, W. Jiang, N. Cai, H. Xie, F. R. Lin, J. Luo, Q. An, H. Y. Woo, A. K. Y. Jen, *Angew. Chem., Int. Ed.* **2022**, *61*, 202205168.
[5] M. Gao, J. Wu, X. Yuan, C. He, H. Jiang, W. Zhao, C. Duan, Y. Chen, Y. Ke, H. Yao, L. Ye, *Energy Environ. Sci.* **2023**, *16*, 5822.
[6] Z. Luo, W. Wei, R. Ma, G. Ran, M. H. Jee, Z. Chen, Y. Li, W. Zhang, H. Y. Woo, C. Yang, *Adv. Mater.* **2024**, *36*, 2407517.
[7] R. Zhang, H. Chen, T. Wang, L. Kobera, L. He, Y. Huang, J. Ding, B. Zhang, A. Khasbaatar, S. Nanayakkara, J. Zheng, W. Chen, Y. Diao, S. Abbrent, J. Brus, A. H. Coffey, C. Zhu, H. Liu, X. Lu, Q. Jiang, V. Coropceanu, J.-L. Brédas, Y. Li, Y. Li, F. Gao, *Nat. Energy* **2024**, *10*, 124.
[8] C. Li, J. Song, H. Lai, H. Zhang, R. Zhou, J. Xu, H. Huang, L. Liu, J. Gao, Y. Li, M. H. Jee, Z. Zheng, S. Liu, J. Yan, X.-K. Chen, Z. Tang, C. Zhang, H. Y. Woo, F. He, F. Gao, H. Yan, Y. Sun, *Nat. Mater.* **2025**, *24*, 433.
[9] J. Fu, Q. Yang, P. Huang, S. Chung, K. Cho, Z. Kan, H. Liu, X. Lu, Y. Lang, H. Lai, F. He, P. W. K. Fong, S. Lu, Y. Yang, Z. Xiao, G. Li, *Nat. Commun.* **2024**, *15*, 1830.
[10] Y. Wang, K. Sun, C. Li, C. Zhao, C. Gao, L. Zhu, Q. Bai, C. Xie, P. You, J. Lv, X. Sun, H. Hu, Z. Wang, H. Hu, Z. Tang, B. He, M. Qiu, S. Li, G. Zhang, *Adv. Mater.* **2024**, *36*, 2411957.
[11] B. Zou, W. Wu, T. A. Dela Pena, R. Ma, Y. Luo, Y. Hai, X. Xie, M. Li, Z. Luo, J. Wu, C. Yang, G. Li, H. Yan, *Nano-Micro Lett.* **2023**, *16*, 30.
[12] N. Wei, J. Chen, Y. Cheng, Z. Bian, W. Liu, H. Song, Y. Guo, W. Zhang, Y. Liu, H. Lu, J. Zhou, Z. Bo, *Adv. Mater.* **2024**, *36*, 2408934.
[13] S. Guan, Y. Li, C. Xu, N. Yin, C. Xu, C. Wang, M. Wang, Y. Xu, Q. Chen, D. Wang, L. Zuo, H. Chen, *Adv. Mater.* **2024**, *36*, 2400342.
[14] Y. Jiang, K. Liu, F. Liu, G. Ran, M. Wang, T. Zhang, R. Xu, H. Liu, W. Zhang, Z. Wei, Y. Cui, X. Lu, J. Hou, X. Zhu, *Adv. Mater.* **2025**, *37*, 2500282.
[15] L. Zhu, M. Zhang, G. Zhou, Z. Wang, W. Zhong, J. Zhuang, Z. Zhou, X. Gao, L. Kan, B. Hao, F. Han, R. Zeng, X. Xue, S. Xu, H. Jing, B. Xiao, H. Zhu, Y. Zhang, F. Liu, *Joule* **2024**, *8*, 3153.
[16] L. Wang, C. Chen, Z. Gan, J. Cheng, Y. Sun, J. Zhou, W. Xia, D. Liu, W. Li, T. Wang, *Adv. Mater.* **2025**, *37*, 2419923.
[17] J. Deng, W. Li, R. Zeng, J. Song, S. Tan, L. Kan, Z. Qin, Y. Zhao, F. Liu, Y. Sun, *Adv. Mater.* **2025**, *37*, 2501243.
[18] L. Liu, H. Li, J. Xie, Z. Yang, Y. Bai, M. Li, Z. Huang, K. Zhang, F. Huang, *Adv. Mater.* **2025**, *37*, 2500352.
[19] H. Chen, Y. Huang, R. Zhang, H. Mou, J. Ding, J. Zhou, Z. Wang, H. Li, W. Chen, J. Zhu, Q. Cheng, H. Gu, X. Wu, T. Zhang, Y. Wang, H. Zhu, Z. Xie, F. Gao, Y. Li, Y. Li, *Nat. Mater.* **2025**, *24*, 444.
[20] Y. Jiang, S. Sun, R. Xu, F. Liu, X. Miao, G. Ran, K. Liu, Y. Yi, W. Zhang, X. Zhu, *Nat. Energy* **2024**, *9*, 975.
[21] K. Jin, Z. Xiao, L. Ding, *J. Semicond.* **2021**, *42*, 010502.
[22] C. Han, B. Cheng, Q. Guo, Z. Fu, J. Qiao, S. Cheng, Y. Huo, X. Xia, H. Wang, Y. Fu, X. Guo, X. Lu, X. Hao, Y. Li, M. Zhang, *Adv. Funct. Mater.* **2025**, *35*, 2416381.
[23] J. Gao, N. Yu, Z. Chen, Y. Wei, C. Li, T. Liu, X. Gu, J. Zhang, Z. Wei, Z. Tang, X. Hao, F. Zhang, X. Zhang, H. Huang, *Adv. Sci.* **2022**, *9*, 2203606;
[24] F. Bai, J. Zhang, A. Zeng, H. Zhao, K. Duan, H. Yu, K. Cheng, G. Chai, Y. Chen, J. Liang, W. Ma, H. Yan, *Joule* **2021**, *5*, 1231.
[25] T. L. H. Mai, Z. Sun, S. Kim, S. Jeong, S. Lee, J. Park, C. Yang, *Energy Environ. Sci.* **2024**, *17*, 7435.
[26] H. Lu, W. Liu, G. Ran, Z. Liang, H. Li, N. Wei, H. Wu, Z. Ma, Y. Liu, W. Zhang, X. Xu, Z. Bo, *Angew. Chem., Int. Ed.* **2023**, *62*, 202314420.
[27] D. Qiu, C. Tian, H. Zhang, J. Zhang, Z. Wei, K. Lu, *Adv. Mater.* **2024**, *36*, 2313251.
[28] A. Zeng, X. Ma, M. Pan, Y. Chen, R. Ma, H. Zhao, J. Zhang, H. K. Kim, A. Shang, S. Luo, I. C. Angunawela, Y. Chang, Z. Qi, H. Sun, J. Y. L. Lai, H. Ade, W. Ma, F. Zhang, H. Yan, *Adv. Funct. Mater.* **2021**, *31*, 2102413.
[29] H. Lu, W. Liu, G. Ran, Z. Liang, H. Li, N. Wei, H. Wu, Z. Ma, Y. Liu, W. Zhang, X. Xu, Z. Bo, *Angew. Chem., Int. Ed.* **2023**, *62*, 202314420.
[30] M. Ghasemi, H. Hu, Z. Peng, J. J. Rech, I. Angunawela, J. H. Carpenter, S. J. Stuard, A. Wadsworth, I. McCulloch, W. You, H. Ade, *Joule* **2019**, *3*, 1328.
[31] H. Hu, M. Ghasemi, Z. Peng, J. Zhang, J. J. Rech, W. You, H. Yan, H. Ade, *Adv. Mater.* **2020**, *32*, 2005348.
[32] G. Garcia-Belmonte, J. Bisquert, *Appl. Phys. Lett.* **2010**, *96*, 113301.
[33] J. C. Blakesley, D. Neher, *Phys. Rev. B: Condens. Matter Mater. Phys.* **2011**, *84*, 075210.
[34] Y. Wei, Z. Chen, G. Lu, N. Yu, C. Li, J. Gao, X. Gu, X. Hao, G. Lu, Z. Tang, J. Zhang, Z. Wei, X. Zhang, H. Huang, *Adv. Mater.* **2022**, *34*, 2204718.
[35] F. Zhang, T. Dai, X. Li, M. Li, Y. Liu, D. Wang, D. Xu, R. Hu, *Adv. Funct. Mater.* **2025**, *35*, 2414260.
[36] X. Xu, W. Jing, H. Meng, Y. Guo, L. Yu, R. Li, Q. Peng, *Adv. Mater.* **2023**, *35*, 2208997.
[37] Q. Chen, Z. Bian, Y. Yang, X. Cui, C. Jeffreys, X. Xu, W. Li, Y. Liu, M. Henney, Z. Bo, *Angew. Chem., Int. Ed.* **2024**, *136*, 202405949.
[38] C. Yang, M. Jiang, S. Wang, B. Zhang, P. Mao, H. Y. Woo, F. Zhang, J. Wang, Q. An, *Adv. Mater.* **2024**, *36*, 2305356.
[39] W. A. Memon, Y. Zhu, S. Xiong, H. Chen, H. Lai, Y. Wang, H. Li, M. Li, F. He, *ACS Appl. Mater. Interfaces* **2024**, *16*, 69467.
[40] Y. Wang, Z. Liang, X. Liang, X. Wen, Z. Cai, Z. Shao, J. Zhang, Y. Ran, L. Yan, G. Lu, F. Huang, L. Hou, *Adv. Energy Mater.* **2023**, *13*, 2300524.
[41] A. Mishra, N. N. Bhuyan, H. Xu, G. D. Sharma, *Mater. Adv.* **2023**, *4*, 6031.
[42] H. Zhao, B. Lin, J. Xue, H. B. Naveed, C. Zhao, X. Zhou, K. Zhou, H. Wu, Y. Cai, D. Yun, Z. Tang, W. Ma, *Adv. Mater.* **2022**, *34*, 2105114.
[43] R. Ma, H. Li, T. A. Dela Peña, H. Wang, C. Yan, P. Cheng, J. Wu, G. Li, *Natl. Sci. Rev.* **2024**, *11*, nwae384.
[44] Y. Wang, C. Gao, W. Lei, T. Yang, Z. Liang, K. Sun, C. Zhao, L. Chen, L. Zhu, H. Zeng, X. Sun, B. He, H. Hu, Z. Tang, M. Qiu, S. Li, P. Han, G. Zhang, *Nano-Micro Lett.* **2025**, *17*, 206.
[45] Y. Ge, Y. Wu, Y. Hai, X. Li, T. Pan, T. A. Dela Peña, J. Wu, Y. Li, H. Yang, C. Cui, Y. Li, *Adv. Mater.* **2025**, *37*, 2502579.
[46] R. Lin, Z. Luo, Y. Wang, J. Wu, T. Jia, W. Zhang, X. Gu, Y. Liu, L. Xiao, Y. Min, *Chem. Eng. J.* **2025**, *503*, 158635.
[47] H. Zhao, B. Lin, J. Xue, H. B. Naveed, C. Zhao, X. Zhou, K. Zhou, H. Wu, Y. Cai, D. Yun, Z. Tang, W. Ma, *Adv. Mater.* **2022**, *34*, 2105114.
[48] Y. Cheng, H. Li, X. Zhang, Y.-N. Chen, G. Ran, Y. Yue, N. Wei, X. Zhu, X. Yan, Y. Liu, H. Lu, Y. Liu, Y. Wei, W. Zhang, Z. Bo, *Adv. Funct. Mater.* **2025**, *35*, 2415468.
[49] Z. Wang, Y. Hu, T. Xiao, Y. Zhu, X. Chen, L. Bu, Y. Zhang, Z. Wei, B. B. Xu, G. Lu, *Adv. Opt. Mater.* **2019**, *7*, 1900152.
[50] L. Bu, S. Gao, W. Wang, L. Zhou, S. Feng, X. Chen, D. Yu, S. Li, G. Lu, *Adv. Electron. Mater.* **2016**, *2*, 1600359.
[51] S. Gao, L. Bu, Z. Zheng, X. Wang, W. Wang, L. Zhou, J. Hou, G. Lu, A. I. P. Adv, **2017**, *7*, 045312.
[52] A. K. Kyaw, D. H. Wang, D. Wynands, J. Zhang, T.-Q. Nguyen, G. C. Bazan, A. J. Heeger, *Nano Lett.* **2013**, *13*, 3796.
[53] G. J. Wetzelaer, M. Scheepers, A. M. Sempere, C. Momblona, J. Avila, H. J. Bolink, *Adv. Mater.* **2015**, *27*, 1837.
[54] K. Cho, J. Kim, S. Y. Yoon, K. Y. Ryu, S.-R. Jang, B. Lim, K. Kim, *Macromol. Rapid Commun.* **2018**, *39*, 1700630.

[55] Z. Zhao, J. Zhao, S. Chung, K. Cho, W. Xu, Z. Kan, *ACS Mater. Lett.* **2023**, *5*, 1718.
[56] N. Schopp, H. M. Luong, B. R. Luginbuhl, P. Panoy, D. Choi, V. Promarak, V. V. Brus, T.-Q. Nguyen, *ACS Energy Lett.* **2022**, *7*, 1626.
[57] Z. Ge, J. Qiao, J. Song, X. Li, J. Fu, Z. Fu, J. Gao, X. Tang, L. Jiang, Z. Tang, G. Lu, X. Hao, Y. Sun, *Adv. Energy Mater.* **2024**, *14*, 2400203.
[58] Y. Lin, Y. Firdaus, F. H. Isikgor, M. I. Nugraha, E. Yengel, G. T. Harrison, R. Hallani, A. El-Labban, H. Faber, C. Ma, X. Zheng, A. Subbiah, C. T. Howells, O. M. Bakr, I. McCulloch, S. D. Wolf, L. Tsetseris, T. D. Anthopoulos, *ACS Energy Lett.* **2020**, *5*, 2935.
[59] H. Huang, G. Zhang, C. Xie, Z. Li, Q. Bai, B. He, M. Qiu, P. Han, H. Hu, S. Li, G. Zhang, *Adv. Funct. Mater.* **2025**, *35*, 2414844.